Program Digest, 2019 IEEE International Ultrasonics Symposium (IUS)
Glasgow, Scotland, October 6-9, 2019

4D Cardiac Activation Wave Mapping in In Vivo Swine Model using Acoustoelectric Imaging

Alexander Alvarez
Deparment of Biomedical Engineering
University of Arizona
Tucson, AZ, USA
alexanderalvarez@email.arizona.edu

Cameron Wilhite
Department of Medical Imaging
University of Arizona
Tucson, AZ, USA
cwilhite@email.arizona.edu

Chet Preston
Department of Biomedical Engineering
University of Arizona
Tucson, AZ, USA
cpreston@email.arizona.edu

Teo Trujillo
Department of Biomedical Engineering
University of Arizona
Tucson, AZ, USA
tetrujillo@email.arizona.edu

Alice McArthur
Sarver Heart Center
University of Arizona
Tucson, AZ, USA
alicem@email.arizona.edu

Debbie Mustacich
Department of Surgery
University of Arizona
Tucson, AZ, USA
debbiem@email.arizona.edu

Russell S. Witte
Department of Medical Imaging
University of Arizona
Tucson, AZ, USA
rwitte@email.arizona.edu

***Abstract*—Though atrial fibrillation (AF) is a growing public health problem, electrical characterization of the disease with electrocardiography (ECG) is inadequate due to poor spatial resolution. The goal of this study was to investigate propagation of the cardiac activation wave in a healthy swine model using acoustoelectric cardiac imaging (ACI), a noninvasive mapping technology that combines ultrasound with electrical recording to overcome limitations with standard ECG. Real-time 4D ACI with a custom 2D 0.6 MHz matrix US array demonstrated conduction velocities of 2.21 m/s, validated with standard epicardial recording. ACI FWHM at a single timepoint, a measure related to the resolution of ACI in imaging the volume of activation at peak ECG signal, was 7.31 mm, 7.63 mm, and 6.23 mm in the depth, lateral, and elevational directions, respectively. SNR of ACI was 21dB at peak activation. ACI signals tracked through a 4D volume demonstrated appropriate propagation of the signal from base to apex and from endocardium to epicardium. This study demonstrated the potential for this technology to noninvasively map arrhythmias, such as AF, at high resolution.**

Keywords — atrial fibrillation, cardiac mapping, arrhythmia, echocardiography, electrocardiography

I. Introduction

A. Clinical Motivation

Atrial Fibrillation (AF) is the most common arrhythmia worldwide and its prevalence is increasing, affecting aging populations around the globe [1]. While AF often arises from hyperactivity in the pulmonary veins, pathology can follow many different sources of electrical and mechanical dysfunction [2]. 12-lead electrocardiography (12-ECG) is typically used to diagnose AF and direct pharmacological or interventional treatment for disease [2]. However, because ECG relies on an inverse problem of only 12 leads placed distant from the heart to localize current sources, it lacks spatial resolution to determine electrical mechanisms of disease and lacks mechanical information altogether. As such, treatment of AF is often nonspecific and inappropriate for individual patients, resulting in complications like stroke. Thus, there exists a need for an imaging technique that can map the electromechanical dynamics of AF with high spatial and temporal resolution. Acoustoelectric cardiac imaging (ACI) – a technology based on the acoustoelectric (AE) effect – promises to accomplish this.

Supported by NIH R24MH109060, R43HL144327 (Electrosonix LLC Subaward), T32EB00809, T32HL007955

B. Acoustoelectric Imaging Theory

The AE effect is a physical interaction that occurs when a pressure wave such as ultrasound (US) interacts with an electrically active material [3]. This interaction causes a change in resistivity $\Delta\rho$ of that material as described by:

$$\Delta\rho = K_I \rho_0 \Delta P \quad (1)$$

where K_I is an interaction constant defined by material properties of the tissue [4], ρ_0 is the native resistivity, and ΔP is the time and space-varying pressure amplitude. When a current density (J^I) is present in the location of the ultrasound beam, this resistivity change results in a measurable voltage near the frequency of the ultrasound transducer described by:

$$V^{AE}(x,y,z,t) = \iiint -K_I \rho_0 J^L(x,y,z) \bullet J^I(x,y,z,t) \Delta P(x,y,z) dxdydz \quad (2)$$

where J^L is the lead field of the recording electrodes (i.e., electric field if unit charge is passed through recording leads).

Using this principle, we can electronically steer US to multiple focused beam positions and measure the interaction signal at each location. In this way, we build a map of AE signals on the millimeter and millisecond scales, which is proportional to the local underlying current densities.

AE validation was initially shown in imaging high current density phantoms that modeled biological current spread using electrodes or crustacean nerve cords placed in saline [5-6]. This work was then extended to *ex vivo* small animal models to attempt to validate the technology in low signal environments; through these studies, the cardiac activation wave was mapped in both the rat and rabbit hearts [7-9]. In this application, we aim to perform proof-of-concept mapping of the electrical activity of a healthy, open chest, *in vivo* swine model without pacing using a custom 2D US matrix array.

II. Materials and Methods

A. Animal Model

All animal protocols were approved by the Institutional Care and Use Committee (IACUC) at the University of Arizona.

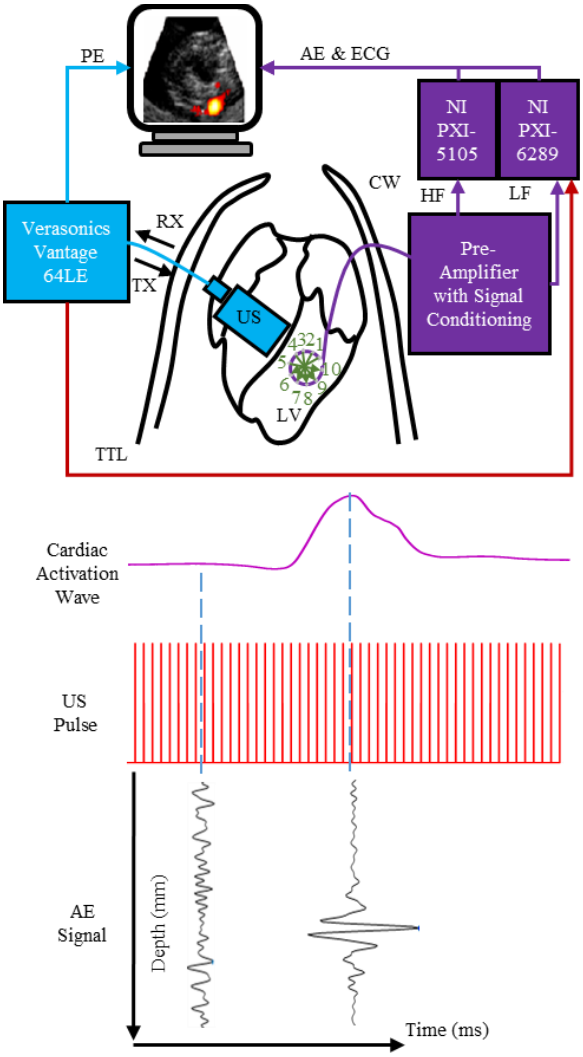

Fig. 1. ACI Setup. (*Top*) Connection Diagram. AE, ECG, and pulse echo data were acquired and processed to produce maps of electrical activity registered on anatomical images. (*Bottom*) Timing Diagram. Ultrasound pulses generated the AE interaction signal and sampled the low frequency cardiac activation waveform. CW = chest wall; LV = left ventricle; RX = receive; TX = transmit; US = 2D ultrasound array; PE = pulse echo data; HF = high frequency signal; LF = low frequency ECG signal; AE = acoustoelectric data.

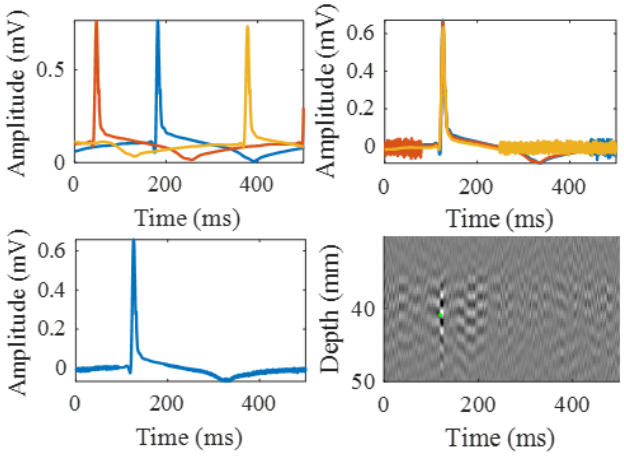

Fig. 2. Post-Averaging Methodology. (*Top Left*) Three low frequency electrogram acquisitions obtained on a single channel of cardiac catheter. A single trace from all acquisitions at a given scan point was chosen as a template. Cross-correlation was performed between each trace and the template. (*Top Right*) The lag associated with the peak correlation was used to shift each trace. Traces were padded with noise outside of the depolarization spike. (*Bottom Left*) All shifted ECG_{LF} at a given scan point were averaged together to increase SNR. This image shows fifteen traces averaged together. (*Bottom Right*) Filtered ECG_{AE} M-Mode signals were shifted same amount and averaged as with ECG_{LF}.

Farm swine of both sexes (N = 11) weighing 50 pounds were obtained from local distributors. After general anesthesia, an open thoracotomy was performed to expose the epicardial surface. Animals were placed on lidocaine CRI to minimize the possibility of arrhythmias during the study.

B. Instrumentation

A custom 0.6 MHz matrix US array was acoustically coupled to the epicardial surface using an adapter to create pulse echo images and generate AE interaction signals (Fig. 1). The array was driven by a Verasonics Vantage 64LE with a pulse repetition frequency (PRF) of 2 to 4 kHz using short pulse excitation and focused US transmission.

A Biosense Webster ecoLasso catheter (ID = 15mm) with 10 leads or a NeuroNexus cardiac surface grid array with 4mm spacing was coupled to the epicardial surface (between the US array and the heart) for recording of both low frequency ECG signals and high frequency AE signals (Fig. 1). Differential leads were created between contacts on the opposite side of the catheter. Signals recorded on each lead were amplified and conditioned by LeCroy differential amplifiers and a custom signal conditioning box. Amplified low frequency signals were digitized via a National Instruments (NI) PXI-6289 DAQ sampled at 20 kHz with 6 V dynamic range; amplified high frequency signals were digitized via an NI PXI-5105 12-bit oscilloscope sampled at 10 MHz with 1 V dynamic range.

Image acquisition proceeded as follows (Fig. 1): 1) The US beam was electronically steered and focused using the Vantage 64LE; 2) An event trigger from a function generator was sent to the Vantage 64LE to begin US transmission sequence at PRF (i.e., 2 to 4 kHz); 3) For each ultrasound pulse, a trigger was sent to the NI, which was armed to record a certain number of samples at 10MHz (corresponding to the depth of the scan), composing a single A-line in fast-time (i.e., μs); 4) Each A-line

was stacked along the slow-time (i.e., ms) axis for a given duration with samples corresponding to the US pulse period; 5) The NI sent a trigger to the Vantage 64 LE when it finished streaming this M-Mode data to the hard drive; 6) This sequence was repeated to collect the desired number of averages; 7) The US beam was steered to a new position and the sequence was repeated to collect the desired number of x and y scan points.

C. Image Analysis

In order to improve SNR for these physiologic recordings, signals from each cardiac cycle were retrospectively lined up and averaged together (Fig. 2). High frequency AE (ECG_{AE}) and pulse echo (PE) signals were shifted in slow time (i.e., 500ms sampled at 2-4kHz) to match low frequency ECG signals (ECG_{LF}).

ECG_{LF} and ECG_{AE} signals were then bandpass filtered along the slow time dimension using a Hann window in the frequency domain between 15 and 250 Hz. ECG_{AE} signals were bandpass filtered in fast time using similar Hann windowing between 0.3 and 0.9 MHz. ECG_{AE} was then demodulated to the baseband frequency and the complex envelope was calculated. M-Mode and B-Mode images were generated from the filtered data. Full-width half-maxima were calculated from the width of the envelope at -6 dB from the maximum signal. Propagation velocity of the ECG_{LF} and ECG_{AE} was taken as the distance between electrodes and scan points, respectively, divided by the delay in peak time.

III. Results

ECG_{LF} signals obtained from the 16-electrode cardiac surface grid array are shown in Fig. 3. Each trace demonstrates simultaneous acquisition of local ECG potentials measured on each electrode. By calculating the delay between the peak time on each of these traces, a cardiac conduction wave velocity of 3.5 m/s traveling from apex to base was calculated. High resolution PE images obtained using a commercial US array (Butterfly IQ) coupled to the epicardium show the imaging window and anatomical information obtained with ACI.

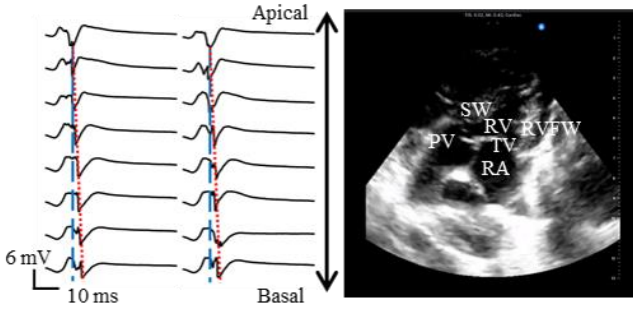

Fig. 3. Standard ECG and PE Imaging on Swine *(Left)* Propagation of Cardiac Activation Wave in Left Ventricular Myocardium. Images help illustrate the propagation of the activation wave from apex to base (blue versus red lines). Peak activation time is delayed on more basal electrodes, demonstrating a conduction velocity of 3.5 m/s. (*Right*) High resolution pulse echo image obtained when coupling commercial US array directly to epicardium, demonstrating images for 0.6 MHz array. SW = septal wall; RVFW = right ventricular free wall; RV = right ventricle; RA = right atrium; PV = pulmonic valve; TV = tricuspid valve.

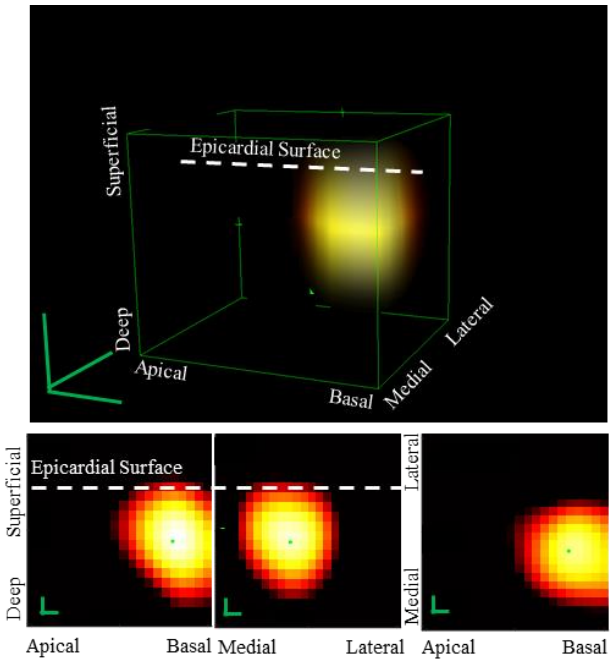

Fig. 4. C-Mode and B-Mode Images of Representative Basebanded ACI Signals at a particular time point (t = 123 ms) (*Top*) Projection of 3D representation of current density of cardiac activation wave. Green bars indicate 5 mm. (*Left*) Lateral-Depth ACI B-Mode Slice at y = -1 mm. (*Middle*) Elevational-Depth ACI B-Mode Slice at x = 2 mm. (*Right*) Lateral-Elevational B-Mode ACI Slice at z = 40.3 mm. Green bars indicate 1 mm. All images shown on a dB-scale (6dB from maximum).

Representative, basebanded 4D images are displayed in Fig. 4. Using ImageJ, a 3D rendering of the AE signal was generated and plotted at the peak of the low frequency signal (corresponding to the depolarization of the ventricle). 2D B-Mode ACI slices (magnitude/envelope) at this point were also generated. The FWHMs of AE signal at -6 dB were calculated as 7.31 mm, 7.63 mm, and 6.23 mm in the depth, lateral, and elevational directions, respectively.

Fig. 5 demonstrates the capability of mapping the cardiac activation wave with ACI. The AE signal is displayed over slow time at the given 3D spatial coordinates. The peak activation time was determined for five sets of three cardiac cycles. The mean and standard error of the peak time across the five sets was calculated to determine the propagation velocity. Using the slope of the best-fit line, this propagation velocity was 2.21 m/s.

Fig. 6 exhibits the propagation of the activation wave by displaying ACI at different time points ("frames"). As shown, the centroid of the basebanded 3D ACI signal shifts laterally and in depth with subsequent frames.

IV. Discussion

This study was the first to validate real-time acoustoelectric cardiac imaging (ACI) in an *in vivo* large animal. The similarity of swine cardiac physiology to humans has been previously described, indicating the promise of ACI to map real-time electrical activity in humans. As shown in Fig. 4, the technology is capable of mapping complex 4D cardiac volumetric activation with ~ 2 mm resolution, demonstrating a

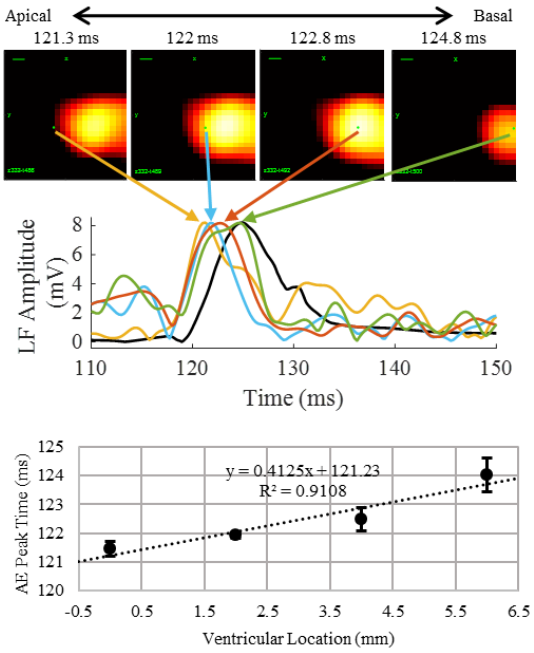

Fig. 5. (*Top*) Propagation of cardiac signal from apex to base. ECG_{AE} taken at different XY (i.e., apical-basal) positions demonstrates a time delay in the peak of the AE signal. Black trace is filtered LF signal. (*Bottom*) LV Location vs AE Peak Time (0 is most apical). AE Peak signal determined at each beam position. Mean of five separate peak measurements taken and error reported as SEM.

significant improvement over standard ECG. Such resolution would help better delineate sources of AF arising throughout the entire atrium.

Comparing results depicted in Fig. 5 to those in Fig. 2, similar signal propagation can be observed; the conduction velocity of ECG_{LF} measurements with high-density electrodes of 3.5 m/s is comparable to the ECG_{AE} measurements of 2.1 m/s. Additionally, these conduction velocities are consistent with previous physiological studies of cardiac activation in the left ventricular free wall [10]. As exhibited in Fig. 6, in addition to mapping the propagation of cardiac signals in the x and y direction over time, with ACI, we also gain critical information about the propagation along depth. When extended to a human AF model, understanding the 3D spread of current densities and time dynamics will help physicians better understand where and when altered activity arises.

Although this study was limited in its use of an invasive, left ventricular, healthy model, it could be extended to noninvasive mapping of atrial fibrillation. By changing the beam focus to deeper structures, we could generate similar electrical activation maps as shown in this study. In addition, through the use of a higher frequency array, we could achieve resolutions relevant to obtain noninvasive images of cardiac activation. In addition, low SNR could be mitigated by improvements in instrumentation and signal processing.

In this study, we demonstrated mapping of healthy swine cardiac electrical activity *in vivo*, highlighting the potential of this technology to affect diagnosis and treatment of AF. As we

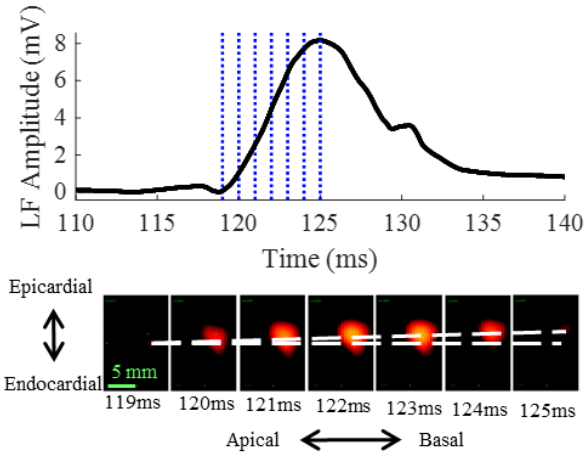

Fig. 6 B-Mode (Lateral-Depth) ACI displayed at different time points. Centroid of signal shifts basally and superficially (i.e., from endocardium to epicardium) with time demonstrating appropriate propagation of signal.

improve our system and combine this information with traditional echocardiography, we will be able to provide clinicians with high spatial and temporal resolution maps of cardiac electrical and mechanical activity, allowing them to treat the mechanism of AF, reaching towards a cure to the underlying pathology that affects millions.

ACKNOWLEDGMENT

The authors would like to thank Pier Ingram for support with Center for Gamma Ray Imaging 3D printed parts and Alice McArthur for help conducting swine surgeries. R.S. Witte has a financial interest in ElectroSonix LLC, which supported this work through a subcontract to the UofA (NIH Phase 1 SBIR).

REFERENCES

[1] H. Zulkifly, G. Y. H. Lip, D. A. Lane, "Epidemiology of Atrial Fibrillation," Int J Clin Practice, vol. 72, pp. e13070, March 2018.

[2] C. Gutierrez, D. Blanchard, "Diagnosis and Treatment of Atrial Fibrillation," Am Fam Phys, vol. 94, pp. 442-452, September 2015.

[3] F. E. Fox, K. F. Herzfeld, G. D. Rock, "The effect of ultrasonic waves on the conductivity of salt solutions," Phys Rev, vol. 70, pp. 329-339, 1946.

[4] Q. Li, R. Olafsson, P. Ingram, Z. Wang, R.S. Witte, "Measuring the acoustoelectric interaction constant in cardiac tissue using ultrasound current source density imaging," Phys Med Biol, vol. 57, pp. 5929-5941.

[5] R. Witte, R. Olafsson, S. Huang, "Imaging current flow in lobster nerve cord using the acoustoelectric effect," Appl Phys Lett, vol. 90, pp. e163902, April 2007.

[6] C. Preston, W. Kasoff, R. S. Witte, "Selective Mapping of Deep Brain Stimulation Lead Currents Using Acoustoelectric Imaging," Ultrasound Med Biol, vol. 44, pp. 2345-2357, November 2018.

[7] Y. Qin, Q. Li, P. Ingram, C. Barber, Z. Liu, R. S. Witte, "Ultrasound Current Source Density Imaging of the Cardiac Activation Wave Using a Clinical Cardiac Catheter," IEEE Trans Bio Eng, vol. 62, pp. 241-247.

[8] R. Olafsson, R. S. Witte, C. Jia, S. Huange, K. Kim, M. O'Donnell, "Cardiac Activation Mapping Using Ultrasound Current Source Density Imaging (UCSDI), IEEE Trans UFFC, vol. 56, pp. 565-575, March 2009.

[9] B. Berthon, P. Dansette, M. Tanter, M. Pernot, J. Provost, "An integrated and highly sensitive ultrafast acoustoelectric imaging system for biomedical applications," Phys Med Bio, vol. 62, pp. 5808-5822, 2017.

[10] M. H. Draper, M. Mya-Tu, "A comparison of the conduction velocity in cardiac tissues of various mammals," Q J Exp Phys Cog Med Sci, vol. 44, pp. 91-109, July 1958.